Materials Transactions, Vol. 42, No. 8 (2001) pp. 1509 to 1516
Special Issue on Nano-Metals I

Formation of Nanocrystals by Crystallisation of Zr–Al–Cu–Ni–Fe Metallic Glasses

Norbert Mattern, Stefan Roth, Uta Kühn, Matthias Hofman, Hans-Dietrich Bauer and Jürgen Eckert

Institut für Festkörper- und Werkstofforschung Dresden, Postfach 27 00 16, D-01171 Dresden, Germany

The influence of iron addition on the crystallisation behaviour of $Zr_{65}Al_{7.5}Cu_{17.5}Ni_{10}$ bulk metallic glass was investigated by differential scanning calorimetry, (DSC), X-ray diffraction, (XRD), transmission electron microscopy, (TEM) and magnetisation measurements. The amorphous $Zr_{65}Al_{7.5}Cu_{17.5}Ni_{10}$ alloy crystallises eutectically into $CuZr_2$ and Zr_6NiAl_2. Addition of iron in amorphous $(Zr_{65}Al_{7.5}Cu_{17.5}Ni_{10})_{100-x}Fe_x$ ($0 \leq x \leq 20$) leads to a changed crystallisation sequence and to the formation of nanocrystals. The formation of a cubic $NiTi_2$-type phase (S.G. $Fd\bar{3}m$, $a_o = 1.22$ nm) is the first step of crystallisation in amorphous alloys with iron contents $x \geq 1$. Depending on the iron content the average crystallite size decreases to the nanometer regime. Ultrafine nanoclusters of down to 2 nm in size are formed as the first step of crystallisation for amorphous $Zr_{52}Al_6Cu_{14}Ni_8Fe_{20}$ due to a high nucleation rate combined with a low growth velocity. The clusters grow by Ostwald ripening during isothermal annealing up to 5 nm average crystallite size. The magnetic behaviour of the $(Zr_{65}Al_{7.5}Cu_{17.5}Ni_{10})_{100-x}Fe_x$ alloys is dominated by temperature-independent Pauli paramagnetism for $x \leq 15$. For $x = 20$, a small contribution of magnetic clusters is observed. These ferromagnetic clusters are in accordance with statistic composition fluctuations within the homogeneous amorphous phase. With the formation of nanocrystals the size of the magnetic clusters increases to the same order of magnitude.

(Received February 20, 2001; Accepted May 14, 2001)

Keywords: *nanocrystalline materials, metallic glass, crystallisation, zirconium-aluminium-copper-nickel-alloys*

1. Introduction

Crystallisation of an amorphous precursor is a possible route to prepare nanocrystals if a high nucleation rate is combined with a low growth rate. For example, this can be achieved by the addition of elements like Au or Nb in Fe-based metallic glasses.[1)] Compared to the amorphous alloy the nanocrystalline state may offer improved properties as it was found for nanocrystalline soft magnetic alloys.[2)] Recently, bulk metallic glasses with good magnetic properties were reported,[3,4)] but further development of such materials requires more fundamental research concerning phase diagrams and phase formation from the amorphous or supercooled liquid state. Nanocrystalline composites with high strength have also been obtained upon crystallisation of Zr-based bulk glasses containing different additions such as Ti or Pd.[5,6)]

In this paper we report on the crystallisation behaviour of a $Zr_{65}Al_{7.5}Cu_{17.5}Ni_{10}$ bulk glass originally developed by Inoue *et al.*[7)] which was modified by iron additions. The influence of the iron content on the phase formation and the magnetic properties was studied in detail. The possibility of formation of an ultrafine nanocrystalline microstructure in this Zr-based system will be shown.

2. Experimental Details

Amorphous $(Zr_{65}Al_{7.5}Cu_{17.5}Ni_{10})_{100-x}Fe_x$ ($0 \leq x \leq 20$) ribbons 10 mm in width and 25 μm in thickness were prepared by means of rapid quenching from the melt using a single-roller melt-spinner under argon atmosphere. For alloys with iron contents > 20 at% no glassy state could be obtained. The thermal behaviour was investigated in a Netzsch DSC 404 differential scanning calorimeter with a heating rate of 40 K/min. Pieces of the ribbons were isothermally annealed at different temperatures T_A under argon atmosphere. X-ray diffraction (XRD) patterns of the annealed samples were recorded by means of a Philips PW 3020 Bragg-Brentano diffractometer using CuKα radiation. For transmission electron microscopy (TEM) investigations, the ribbons were thinned by ion beam sputtering using Ar at 5 keV at grazing incidence. TEM images and electron diffraction patterns were obtained using a Tecnai F30 microscope. The magnetisation was measured as a function of the external field and the temperature using a SQUID-magnetometer. The temperature ranged from 1.5 to 300 K and the field varied between −5 T and +5 T.

3. Results and Discussion

3.1 Thermal behaviour and phase formation

Figure 1 shows the thermal behaviour of the as-spun ribbons with different Fe content as obtained from the DSC traces. The amorphous $Zr_{65}Al_{7.5}Cu_{17.5}Ni_{10}$ alloy crystallises via a single exothermic event into tetragonal $CuZr_2$ and hexagonal Zr_6NiAl_2 (as determined by XRD measurements). In detail, the crystallisation mode is rather complicated. A cubic phase of the $NiTi_2$-type is formed as a metastable intermediate phase depending on the temperature-time regime applied for annealing.[8)] On the other hand, the crystallisation behaviour as well as the phases formed are strongly influenced by oxygen impurities.[9,10)] Recently, Saida *et al.*[11)] reported the observation of the primary formation of this so-called "big cube phase" after annealing of amorphous $Zr_{65}Al_{7.5}Cu_{17.5}Ni_{10}$ containing 0.04% oxygen at 740 K for 120 s. With the incorporation of iron into amorphous $Zr_{65}Al_{7.5}Cu_{17.5}Ni_{10}$ the crystallisation behaviour is changed as indicated by two or three peaks in the DSC traces. Figure 2 shows the dependence of the transformation temperatures versus the iron content x for the $(Zr_{65}Al_{7.5}Cu_{17.5}Ni_{10})_{100-x}Fe_x$ alloys (the glass transition temperature T_g and the crystallisation temperature T_{x1} are defined as the onset temperatures

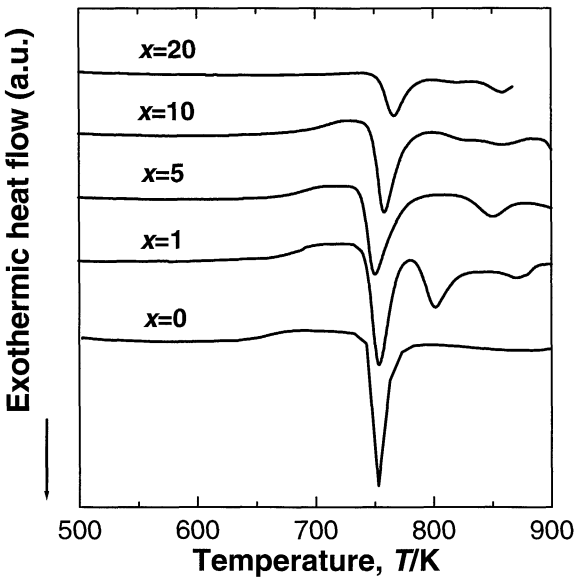

Fig. 1 DSC scans of amorphous $(Zr_{65}Al_{7.5}Cu_{17.5}Ni_{10})_{100-x}Fe_x$ alloys with varying Fe content.

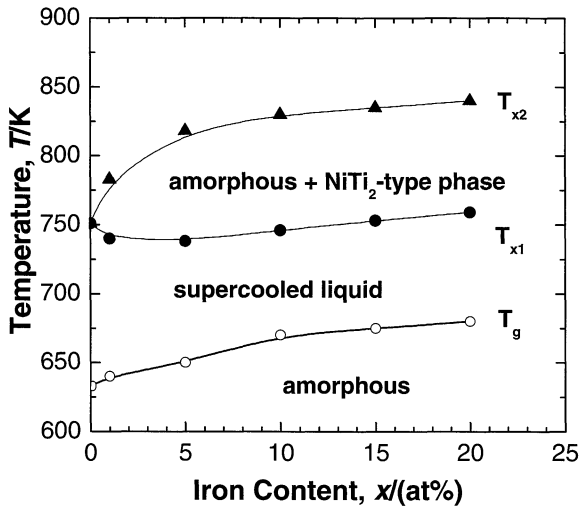

Fig. 2 Thermal behaviour of amorphous $(Zr_{65}Al_{7.5}Cu_{17.5}Ni_{10})_{100-x}Fe_x$.

of the glass transition and the first crystallisation peak, respectively). The glass transition temperature continuously increases with increasing iron content from 633 K for $x = 0$ to 688 K for $x = 20$. For $x = 20$, there is still a supercooled region $\Delta T_x = T_{x1} - T_g$ of about 40 K. For all the iron-containing alloys, the cubic phase of the $NiTi_2$-type (S.G. 227) forms in the first step of crystallisation. The temperature window where this metastable phase exists becomes extended with increasing iron content. Obviously, the addition of iron stabilises the metastable "big cube phase". Figure 3 shows as an example the XRD patterns of the $(Zr_{65}Al_{7.5}Cu_{17.5}Ni_{10})_{80}Fe_{20}$ alloy obtained after isothermal annealing for 1 hour at different temperatures T_A. For the $(Zr_{65}Al_{7.5}Cu_{17.5}Ni_{10})_{80}Fe_{20}$ alloy the amorphous state remains for annealing temperatures up to $T_A = 698$ K. Annealing at 723 K $\leq T_A \leq$ 773 K leads to the formation of the cubic $NiTi_2$-type phase ($a_0 = 1.22$ nm). The strong broadening of the reflections indicates the formation of a nanocrystalline microstructure.

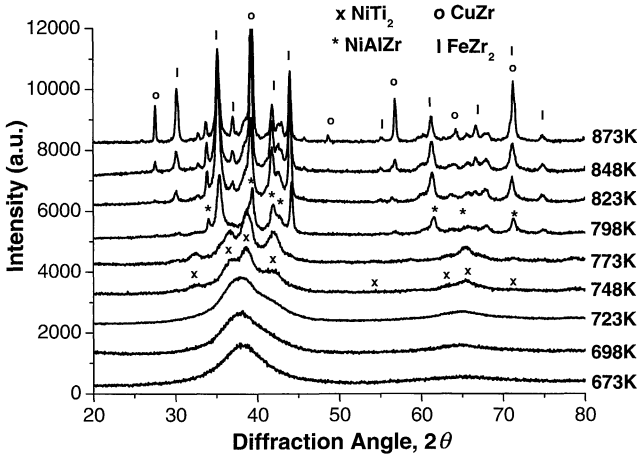

Fig. 3 XRD patterns of $(Zr_{65}Al_{7.5}Cu_{17.5}Ni_{10})_{80}Fe_{20}$ versus annealing temperature at T_A ($t = 1$ h).

The formation of a metastable cubic phase with $NiTi_2$ structure was reported earlier for melt-spun $NiZr_2$ and $CoZr_2$ ribbons[9,12] and, more recently, for bulk glass-forming Zr–Ni–Al–Cu alloys.[8,10,11] The chemical composition of the $NiTi_2$-type phase in the iron containing samples is unknown but probably all elements of the alloy are present. Cubic $NiZr_2$ may have an extended solid solution range between nickel and other metal atomos. In[11] the chemical composition of the $NiTi_2$-type phase was found to differ only slightly from that of the alloy.[11] In our case solution of iron is indicated by the variation of the lattice constant a_0 with the iron content.

At higher temperatures the cubic phase transforms into stable crystalline intermetallic phases. For $x \leq 5$, tetragonal $CuZr_2$ (S.G. 139) and hexagonal Zr_6NiAl_2 (S.G. 189) form in the second step of crystallisation. For $x = 10$, the cubic CuZr phase (S.G. 221) with $a_0 = 0.326$ nm is observed instead of $CuZr_2$. For the $(Zr_{65}Al_{7.5}Cu_{17.5}Ni_{10})_{80}Fe_{20}$ alloy the cubic phase and the remaining amorphous phase transform into a tetragonal $FeZr_2$-type phase (S.G. $I4/mmm$, No. 140) and a cubic NiAlZr phase at $T_A \geq 800$ K. In the next step of crystallisation the equilibrium phases (cubic CuZr and tetragonal $FeZr_2$) are formed (Fig. 3). The crystallisation of the $(Zr_{65}Al_{7.5}Cu_{17.5}Ni_{10})_{100-x}Fe_x$ alloys is determined by nucleation and growth of the corresponding phases. Figure 4 shows the temperature and time dependence of the phase formation for the amorphous $(Zr_{65}Al_{7.5}Cu_{17.5}Ni_{10})_{80}Fe_{20}$ alloy. The crystallisation exhibits a distinct incubation behaviour and the transitions follow an Arrhenius law, typical for thermally activated processes.

3.2 Microstructure

The broadening of the reflections of the cubic $NiTi_2$-type phase was found to be dependent on the iron content as well as on the annealing time and temperature employed. In general, the reflections become wider with increasing iron content for comparable annealing parameters. Figure 5 shows the XRD patterns of $(Zr_{65}Al_{7.5}Cu_{17.5}Ni_{10})_{100-x}Fe_x$ annealed for 30 min at 723 K. Because of the strong overlap of the reflections, Rietveld refinement[13] of the XRD patterns was applied to evaluate the profile using the $NiTi_2$ crystal structure data[14] as parameters assuming Zr at Ti sites, and Al, Cu, Ni, Fe sta-

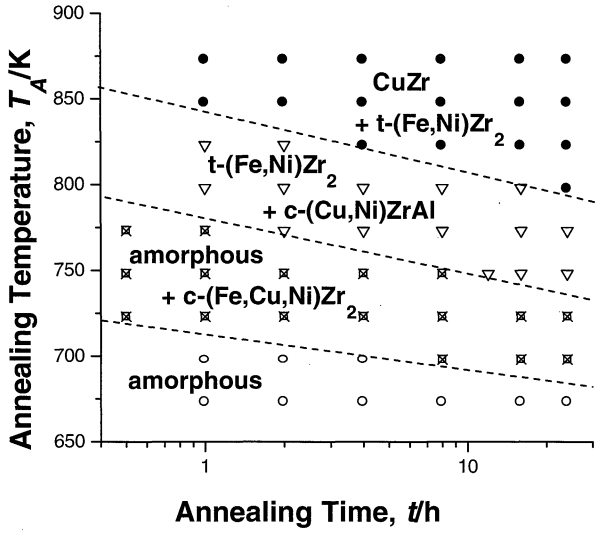

Fig. 4 Phase formation diagram of $(Zr_{65}Al_{7.5}Cu_{17.5}Ni_{10})_{80}Fe_{20}$.

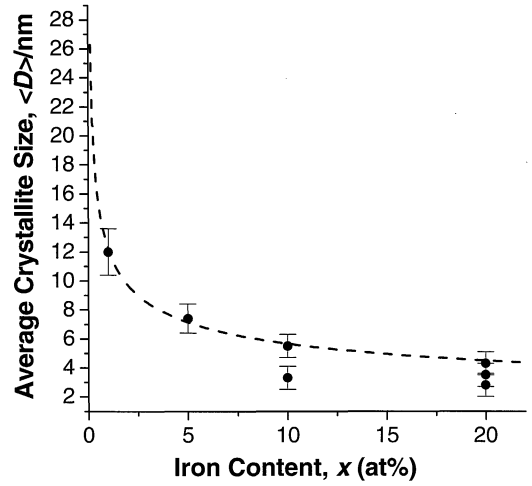

Fig. 6 Average crystallite size $\langle D\rangle$ of annealed $(Zr_{65}Al_{7.5}Cu_{17.5}Ni_{10})_{100-x}Fe_x$.

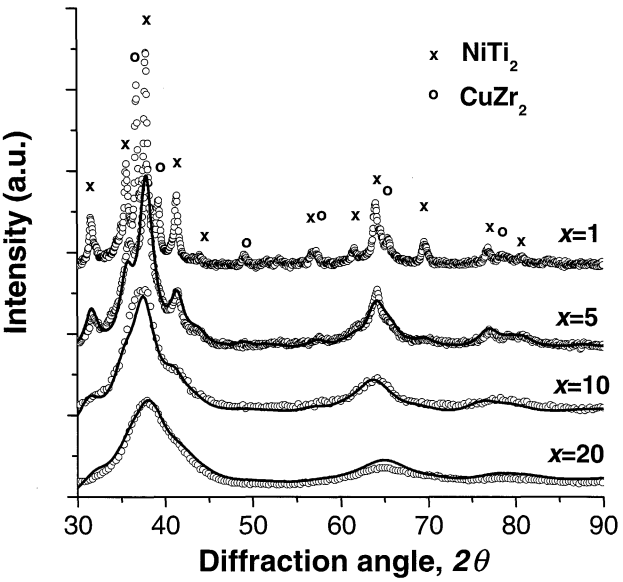

Fig. 5 XRD patterns of $(Zr_{65}Al_{7.5}Cu_{17.5}Ni_{10})_{100-x}Fe_x$ at annealed $T_A = 723$ K for 30 min (measured (◯) and calculated (×) data).

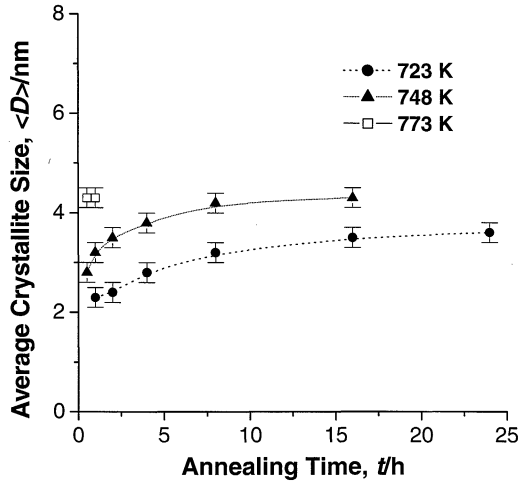

Fig. 7 Average crystallite size $\langle D\rangle$ $(Zr_{65}Al_{7.5}Cu_{17.5}Ni_{10})_{80}Fe_{20}$ versus annealing time.

tistically distributed at Ni sites, respectively. The reflection profiles were approximated by Pseudo Voigt functions using the Caglioti function [13]:

$$B^2 = w + v * \tan\theta + u * \tan^2\theta \qquad (1)$$

to describe the dependence of the peak-width B on the diffraction angle 2θ (u, v, w are fit parameters of the Rietveld refinement). The calculated XRD pattern, are also shown in Fig. 5 by the solid lines. The angle-dependence of the width at half maximum B of reflections indicates that the peak broadening is caused by the size effect only and not by additional strain contributions. The average crystallite size $\langle D\rangle$ was estimated by applying the well-known Williamson-Hall analysis[13]

$$B^2\cos^2\theta = (\lambda/\langle D\rangle)^2 + \langle\varepsilon\rangle\sin^2\theta. \qquad (2)$$

Figure 6 shows the estimated $\langle D\rangle$ values for the samples with different iron contents. The average crystallite size fits well to $\sqrt[3]{x}$ functional behaviour indicating that the number of crystallites N is proportional to the iron content ($N \sim x$). Depending on composition, annealing temperature and annealing time an average crystallite size $\langle D\rangle$ of 2–12 nm is calculated. Several data points in Fig. 6 for a given alloy composition correspond to different annealing parameters.

The time dependence of the average crystallite diameter is shown in Fig. 7 for the alloy $(Zr_{65}Al_{7.5}Cu_{17.5}Ni_{10})_{80}Fe_{20}$. In the case of the sample annealed at 723 K for 1 h a value of $\langle D\rangle \approx 2$ nm is estimated. This means, extremely small crystallites or clusters are formed with a large number of atoms at the surface embedded in the remaining amorphous phase. The crystallites grow upon crystallisation with time and their average diameter saturates at values of about 4–5 nm. Annealing for longer times leads then to the transformation of the $NiTi_2$-type phase as given in Fig. 4.

TEM images of $(Zr_{65}Al_{7.5}Cu_{17.5}Ni_{10})_{80}Fe_{20}$ annealed at 748 K for 1, 2, and 8 hours are shown in Figs. 8(a), (b), and (c). Small ordered regions can be found in the annealed samples as indicted in Figs. 8(a)–(c). The size of these regions becomes larger and lattice planes become visible, more pro-

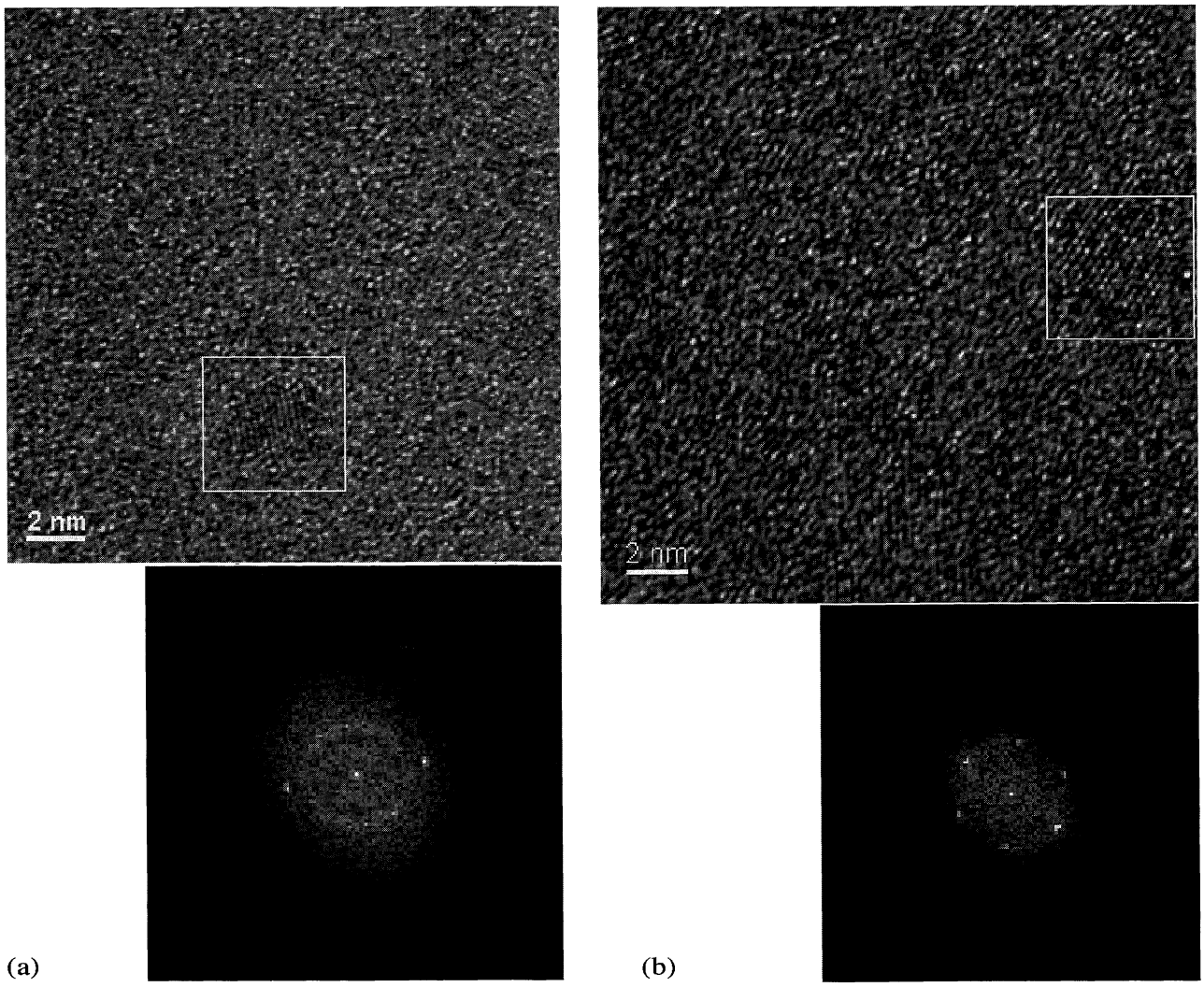

nounced for longer annealing times. The interplanar distances are smaller than the lattice constant of the $NiTi_2$ type phase which means a higher index (*hkl*). (100)-lattice planes with distances of the lattice constant were not observed due to the small size of the crystallites. The presence of areas with ordered states is confirmed by Fast Fourier transforms of the images indicating symmetries. In agreement with the estimation from the XRD data a crystallite size between 2 and 4 nm can be estimated for the $NiTi_2$ type crystallites.

The formation of the ultrafine nanostructure especially in the first stage of crystallisation was studied in more detail. Figure 9 compares the DSC trace of the as-quenched amorphous $Zr_{52}Al_6Cu_{14}Ni_8Fe_{20}$ alloy with those of the annealed states. The sample which was annealed at 723 K for 1 h represents the state after the first exothermic reaction because the first peak has been passed, and the second and third events are identical to those of the as-quenched ribbon. The sample annealed at 748 K for 1 h shows the second exothermal peak partly. Only the third event is visible for the sample after annealing at 773 K for 1 h. A glass transition is visible for all annealed states at a slightly enhanced temperature (T_g = 700–720 K) compared to the as-spun material (T_g = 680 K). This behaviour points to the presence of a remaining amorphous phase in the annealed samples. The corresponding XRD patterns are shown in Fig. 3. The diagram of the 723 K/1 h annealed state differs only slightly from that of the amorphous as-quenched sample. Diffuse, amorphous-like maxima with a shoulder in the first peak and an enhanced intensity in the second maximum are obtained for the state annealed over the first DSC peak. An average crystallite size $\langle D \rangle$ = 4.3 nm is calculated for the sample annealed at 773 K/1 h from the line widths. In the case of the sample annealed at 723 K/1 h there are differences between calculation and measurement as shown in Fig. 5. A value of $\langle D \rangle \approx 2$ nm is obtained by applying the Williamson-Hall analysis. The experimental patterns are reproduced best by a superposition of the diagram of the cubic phase with $NiTi_2$ structure and an amorphous phase. From these fits, the amorphous volume fraction is estimated to be about 40 ± 10 vol% for the samples annealed at 723 or 773 K, respectively. The small size and the presence of amorphous phase mean that a large number of atoms are situated at the surface of the crystals embedded in the remaining amorphous phase. The differences between calculated and experimental XRD patterns which become larger with reduction in size may be caused by these contributions. On the other hand, the diffuse character of the XRD pattern does not allow unique conclusions for this particular structural state.

To characterise the structure development of

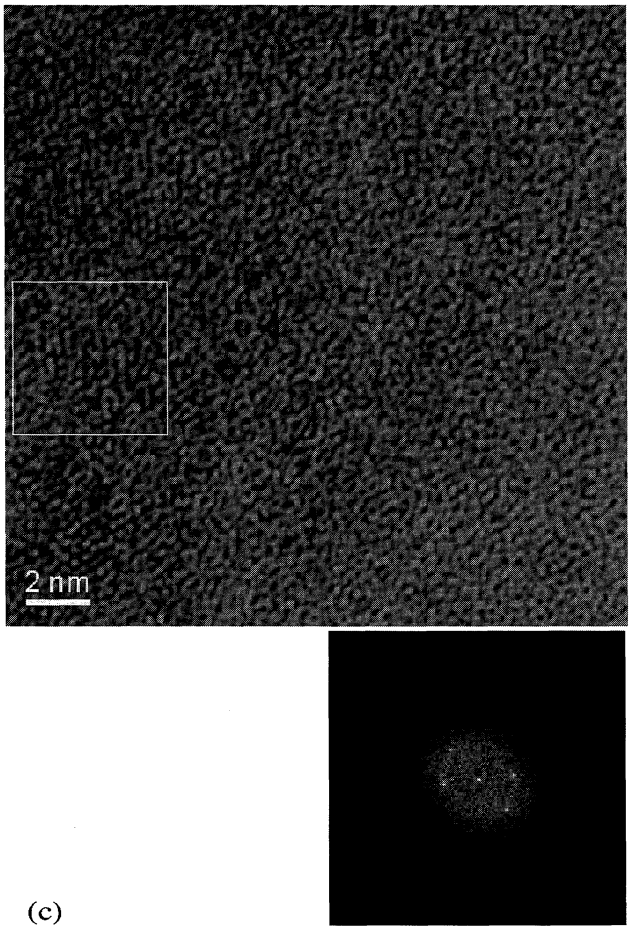

Fig. 8 TEM images of $(Zr_{65}Al_{7.5}Cu_{17.5}Ni_{10})_{80}Fe_{20}$ annealed at 748 K (a) for 1 h, (b) for 2 h, and (c) for 8 h.

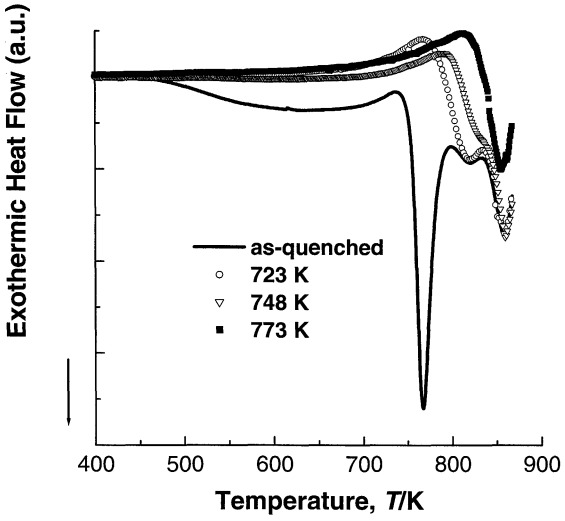

Fig. 9 DSC scans of $(Zr_{65}Al_{7.5}Cu_{17.5}Ni_{10})_{80}Fe_{20}$.

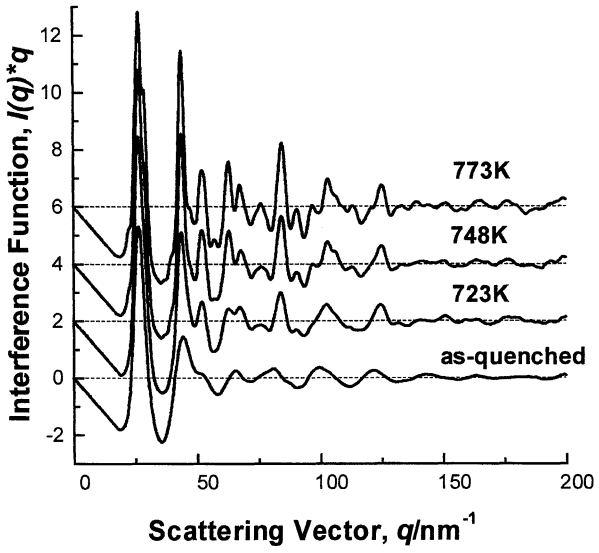

Fig. 10 Interference functions $I(q)$ of $Zr_{52}Al_6Cu_{14}Ni_8Fe_{20}$ vs. annealing.

$(Zr_{65}Al_{7.5}Cu_{17.5}Ni_{10})_{80}Fe_{20}$ upon annealing the scattering curves were measured in a wide q-range ($q = 4\pi \sin\theta/\lambda$) up to 270 nm^{-1} at the high-energy beam-line BW5 of the storage ring DORIS ($\lambda = 0.010776$ nm). Figure 10 shows the corresponding interference functions $I(q)$ as calculated from the elastic scattered XRD intensities. From the interference function $I(q)$ the atomic pair correlation function $g(r) = \rho(r)/\rho_0$ was calculated by the Fourier transform of:[15]

$$4\pi \cdot r \cdot \rho_0 \cdot (g(r) - 1) = \frac{2}{\pi} \cdot \int I(s) \cdot s \cdot \sin(s \cdot r) \cdot ds \quad (3)$$

where $\rho(r)$ is the radial atomic pair density distribution function and $\rho_0 = 53\ nm^{-3}$ is the mean atomic density. Figure 11

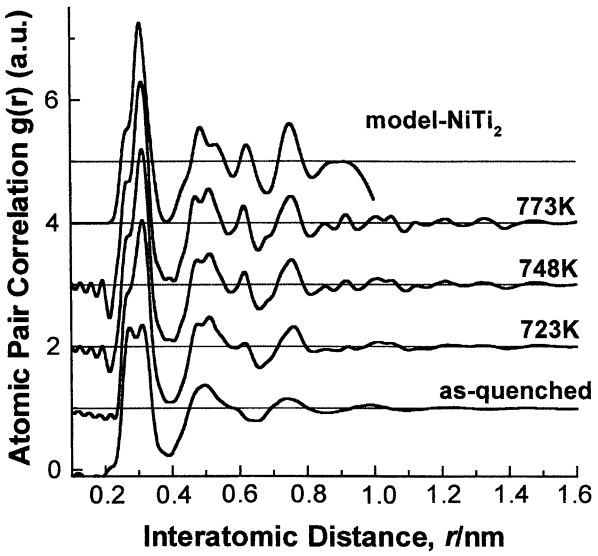

Fig. 11 Atomic pair correlation function $g(r)$ of $(Zr_{65}Al_{7.5}Cu_{17.5}Ni_{10})_{80}Fe_{20}$ vs. annealing.

shows the calculated $g(r)$ curves. For all these curves two components of the first maximum in $g(r)$ are visible. The second maximum consists of at least three components. The peak positions of the first maximum can be attributed to the zirconium-metal ($r^1_{Zr-M} = 0.27$ nm) and the zirconium-zirconium ($r^1_{Zr-Zr} = 0.31$ nm) distances which correspond to the values in crystalline MZr_2 and MZr phases.[13] The heights of the components of $g(r)$ change upon annealing. This behaviour clearly indicates a complete change of the short-range order of an essential volume fraction after annealing at 723 K. The short-range order is found to be rather similar for all annealed states. To compare the short-range order with that of the $NiTi_2$-type phase a model for a quasicrystalline approximation of the amorphous structure was applied.[16] Figure 11 shows the calculated total X-ray pair correlation function $g(r)$. The short-range order of the cubic $NiTi_2$-type phase is found to be similar to the experimental curves of the annealed states, but clearly different to that of the amorphous as-quenched state. On the other hand, the short-range order of tetragonal $CuZr_2$, and of tetragonal (Fe, Ni)Zr_2 is quite different from those of the experimental results. With increasing annealing temperature T_a the oscillations in $g(r)$ become more extended to higher r-values. If we calculate the correlation length r_c, (the value where deviations of $g(r)$ become less then 1% from the average density), then we get $r_c = 1.4$ nm for the as quenched state, $r_c = 1.8$ nm for the 723 K annealed state, and $r_c = 3.0$ nm for the 773 K annealed state, respectively. The first stage of crystallization of amorphous $(Zr_{65}Al_{7.5}Cu_{17.5}Ni_{10})_{80}Fe_{20}$ is, therefore, nucleation with complete rearrangement of the atoms to form clusters without remarkable growth. Most likely, this is related to significant chemical redistribution for the formation of the $NiTi_2$ type nanocrystals. The primary precipitation of clusters corresponds to the first exothermic reaction of the DSC scan. The second peak in the DSC is related to the growth of the clusters. Because the volume fraction of the amorphous phase does not change with time and temperature as proven from fits we conclude that the growth mechanism is Ostwald ripening. The third DSC peak in Fig. 9 at an onset temperature of about 800 K is correlated to the transformation of the metastable $NiTi_2$-type phase and the crystallization of the remaining amorphous phase into tetragonal (Fe, Ni)Zr_2 and cubic (Cu, Ni)ZrAl phases as can be seen from Figs. 3 and 4.

3.3 Magnetic properties

The measurements of the magnetisation of the amorphous as-quenched samples as a function of the applied magnetic field show neither any remanent magnetisation nor a magnetic hysteresis in the investigated composition range of the samples. Thus, ferromagnetism and spin glass behaviour can be excluded, and only positive fields are discussed further. Measurements of the temperature dependence of the magnetisation at 0.1 T for $x < 20$ show low and nearly constant values. The susceptibility is about 2×10^{-6} cm^3/g for $x = 5$. Such a behaviour may be interpreted as temperature independent Pauli paramagnetism of conduction electrons. The magnetisation of the $x = 20$ alloy differs completely in size as well as in temperature dependence. Figure 12 shows the magnetisation of as-quenched of $Zr_{52}Al_6Cu_{14}Ni_8Fe_{20}$ as a function of the magnetic field for different temperatures. The magnetisation fits well to

$$M(H)/M(5\,T) = \chi^0_{\text{para}} * H + a_0 \int_{1\mu_B}^{\mu_{\max}} L\left(\frac{\mu H}{k_B T}\right) d\mu \quad (4)$$

where $L(x) = \coth(x) - 1/x$ is the Langevin function. $\chi_{\text{para}} = \chi^0_{\text{para}} * M(5\,T)$ may be interpreted as a paramagnetic susceptibility. The second term describes the field and temperature dependence of a set of magnetic clusters whose moments are equally distributed between 1 μ_B and $\mu_{\max}$, and no interaction between the clusters is presumed. The magnetic results for the alloy with $x = 20$ suggest, that there is ferromagnetic coupling of the Fe atoms within a given cluster, whereas the interaction between the clusters is negligible. The ferromagnetic clusters are very small (number of iron atoms $N_{Fe} \approx 100$) and have a low volume fraction. About 0.04% of the iron atoms are located in magnetic clusters. An analysis of the distribution statistics of Fe atoms arranged in random packing of spheres gives a certain probability of clusters of a given size. For $x = 20$, a value of 0.04 Fe in clusters with ≥ 100 atoms can be estimated in agreement with the magnetic measurements. On the other hand, clusters with $N_{Fe} \leq 100$ are non-magnetic.[11]

The magnetisation of $(Zr_{65}Al_{7.5}Cu_{17.5}Ni_{10})_{80}Fe_{20}$ annealed at 748 K for 30 min was measured as a function of field at three different temperatures (5 K, 15 K, and 45 K). In contrast to the as-quenched samples, the magnetisation as a function of the field for some of the annealed samples shows a remanent magnetisation and magnetic hysteresis. The values of the reduced remanent magnetisation are given in Table 1. Thus, upon annealing ferromagnetism develops. The longer the annealing time and the lower the measuring temperature are, the higher is the remanent magnetisation. For the samples annealed at 748 K for annealing times ≥ 12 h, the tetragonal (Fe, Ni)Zr_2-phase forms. That is, at low temperatures and after long annealing times the system cannot be considered to be superparamagnetic as in the as-quenched state. In Table 2 the values for the average magnetic moment according to the

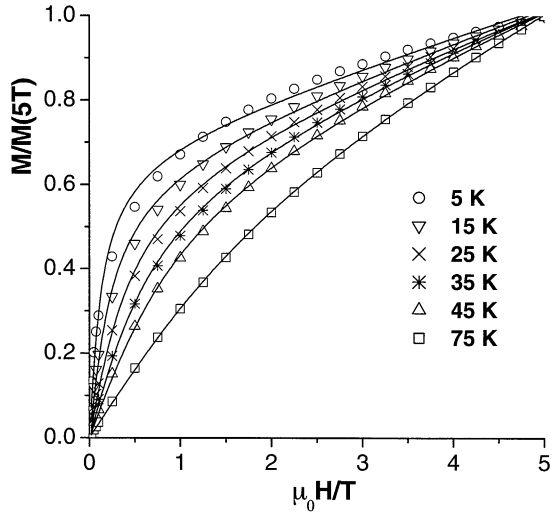

Fig. 12 Magnetisation curves of amorphous $(Zr_{65}Al_{7.5}Cu_{17.5}Ni_{10})_{80}Fe_{20}$.

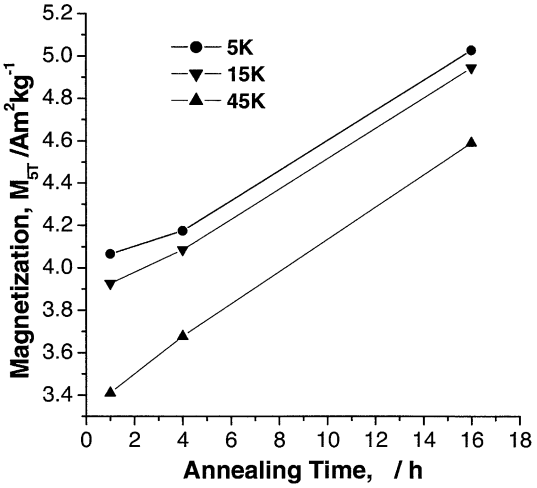

Fig. 13 Magnetic moment of $(Zr_{65}Al_{7.5}Cu_{17.5}Ni_{10})80Fe_{20}$ vs. annealing time.

Table 1 Reduced remanent magnetization M_r/M_{5T} for $(Zr_{65}Al_{7.5}Cu_{17.5}Ni_{10})_{80}Fe_{20}$.

T_{meas}	5 K	15 K	45 K
t_{anneal}			
1 h	0	0	0
4 h	0.08	0	0
16 h	0.36	0.28	0.10

Table 2 Apparent average magnetic moment in μ_{Bohr} for $(Zr_{65}Al_{7.5}Cu_{17.5}Ni_{10})_{80}Fe_{20}$.

	5 K	15 K	45 K
0 h	113	171	141
1 h		631	516
4 h		1078	1196

fit to eq. (4) are given. The apparent magnetic moment in a perfect superparamagnet should be independent of temperature. In our case, we expect that the magnetic moments of the clusters decrease with increasing temperature as in a normal ferromagnet. At low temperatures the interaction between the moments is no longer negligible and the model of noninteracting clusters is no more applicable. The temperature dependence of the apparent average magnetic moment between 15 K and 45 K is not very large for the samples annealed for 0, 1, and 4 h. Thus, their values may be used to estimate a cluster size of about 150, 570, and 1140 atoms ($5 \times 5 \times 5 = 1\,nm^3$, $8 \times 8 \times 8 = 2\,nm^3$, $10 \times 10 \times 10 = 2.5\,nm^3$) after 0, 1 and 4 hours annealing, respectively. The atomic moment is assumed to be 1 μ_B for this estimation. No cluster size can be estimated for the sample annealed for 16 h because there is a remanent magnetisation. This is reflected in the large temperature dependence of the apparent average magnetic moment.

In Fig. 13 the magnetic moment measured at maximum field of 5 Tesla as a function of the annealing time is plotted. There is an increase of the magnetic moment of about 20% if the annealing time increases from 1 to 16 hours. The magnetic cluster size increases by a factor of 10. So it may be assumed that the increase in magnetic cluster size is probably due to redistribution of atoms located in the cluster rather than by an increasing degree of phase separation.

4. Conclusions

Addition of iron in amorphous $(Zr_{65}Al_{7.5}Cu_{17.5}Ni_{10})_{100-x}Fe_x$ ($0 \leq x \leq 20$) leads to a changed crystallisation behaviour. An intermediate cubic $NiTi_2$-type phase (S.G. $Fd\bar{3}m$, $a_o = 1.22\,nm$) is formed as the first step of crystallisation in amorphous alloys with iron contents $x \geq 1$. Ultrafine nanoclusters of down to 2 nm in size are formed upon crystallisation due to a high nucleation rate combined with a low growth velocity. For $x = 20$, a small contribution of magnetic clusters is observed. These ferromagnetic clusters are in accordance with statistic composition fluctuations within the homogeneous amorphous phase. With the formation of nanocrystals the size of the magnetic clusters increases to the same order of magnitude.

Acknowledgements

The authors would like to thank J. Neuefeind for support at the synchrotron measurements, W. Gude, K. Stange, and D. Lohse for technical assistance, and L. Schultz for stimulating discussions.

REFERENCES

1) U. Köster and J. Meinhardt: Mater. Sci. Eng. A **178** (1994) 271–278.
2) Y. Yoshizawa, S. Oguma and K. Yamauchi: J. Appl. Phys. **64** (1988) 6044–6046.
3) A. Inoue, T. Zhang, T. Itoi and A. Takeuchi: Mater. Trans., JIM **38** (1997) 359–362.
4) A. Inoue: Mater. Sci. Eng. A**226-228** (1997) 357–363.
5) C. Fan, A. Takeuchi and A. Inoue: Mater. Trans., JIM **40** (1999) 42–51.
6) C. Fan, D. Louzguine, C. Li and A. Inoue: Appl. Phys. Lett. **75** (1999) 340–342.
7) A. Inoue: Sci. Rep. RITU A**42** (1996) 1–11.
8) N. Mattern, J. Eckert, M. Seidel, U. Kühn, S. Doyle and I. Bächer: Mater. Sci. Eng. A**226-228** (1997) 468–473.
9) Z. Altounian, E. Batalla, J. O. Strøm-Olsen and J. L. Walter: J. Appl. Phys. **61** (1987) 149–155.

10) J. Eckert, N. Mattern, M. Zinkevitch and M. Seidel: Mater. Trans., JIM **39** (1998) 623–632.
11) J. Saida, M. Matsushita and A. Inoue: J. Mater. Res. **16** (2001) 228–231.
12) U. Köster: Mater. Sci. Forum **225-227** (1996) 311–316.
13) R. A. Young: *The Rietveld Method*, Intern. Union of Crystallography, (Oxford University Press, 1993) pp. 1–298.
14) P. Villars and L. D. Calvert, *Pearsons's Handbook of Crystallographic Data for Intermetallic Phases*, (ASM Ohio, 1991) pp. 1–5366.
15) C. N. J. Wagner: *Adv. in X-ray Analysis*, (Plenum Press New York, 1969) pp. 50–71.
16) N. Mattern and H. Hermann: Phys. Status Solidi (b) **104** (1981) 547–554.